Modeling and simulations for molecular scale hydrodynamics of the moving contact line in immiscible two-phase flows

Modeling and simulations for molecular scale hydrodynamics of the moving contact line in immiscible two-phase flows

Tiezheng Qian[1,2,4]**, Congmin Wu**[1]**, Siu Long Lei**[1]**, Xiao-Ping Wang**[1,2] **and Ping Sheng**[3]

[1] Department of Mathematics, Hong Kong University of Science and Technology, Clear Water Bay, Kowloon, Hong Kong
[2] KAUST–HKUST Micro/Nanofluidic Joint Laboratory, Hong Kong University of Science and Technology, Clear Water Bay, Kowloon, Hong Kong
[3] Department of Physics and William Mong Institute of Nano Science and Technology, Hong Kong University of Science and Technology, Clear Water Bay, Kowloon, Hong Kong

E-mail: maqian@ust.hk

Abstract
This paper starts with an introduction to the Onsager principle of minimum energy dissipation which governs the optimal paths of deviation and restoration to equilibrium. Then there is a review of the variational approach to moving contact line hydrodynamics. To demonstrate the validity of our continuum hydrodynamic model, numerical results from model calculations and molecular dynamics simulations are presented for immiscible Couette and Poiseuille flows past homogeneous solid surfaces, with remarkable overall agreement. Our continuum model is also used to study the contact line motion on surfaces patterned with stripes of different contact angles (i.e. surfaces of varying wettability). Continuum calculations predict the stick–slip motion for contact lines moving along these patterned surfaces, in quantitative agreement with molecular dynamics simulation results. This periodic motion is tunable through pattern period (geometry) and contrast in wetting property (chemistry). The consequence of stick–slip contact line motion on energy dissipation is discussed.

(Some figures in this article are in colour only in the electronic version)

1. Introduction

The contact line denotes the intersection of the fluid–fluid interface with the solid wall. When one fluid displaces the other, the contact line moves along the wall (see figure 1). As a classical problem in continuum hydrodynamics, it has been known for decades that the moving contact line (MCL) is incompatible with the no-slip boundary condition [1]—the latter leads to a non-integrable singularity in viscous dissipation [2–5]. This MCL problem is directly related to the study of wetting dynamics: understanding the dynamics of fluids in the vicinity of the MCL is essential to a comprehensive picture for the dynamic wetting behavior of liquids on solid surfaces.

The heart of the MCL problem lies in the boundary condition(s) at the fluid–solid interface. In particular, molecular dynamics (MD) simulations showed that fluid slip indeed occurs at the MCL [6, 7]. Numerous models had been proposed over the years [8–18], but none was able to give a quantitative account of the fluid slip measured in MD simulations. In fact, there has been a lasting debate over the boundary conditions for a fluid flowing past a solid surface. In recent years, the Newtonian flows in confined geometries have received much attention, and numerous research efforts have shown that fluid slip occurs at the solid boundary in many circumstances [19, 20].

MD simulations have proven to be instrumental in investigating the fluid dynamics in the molecular scale vicinity of the MCL. Through analysis of extensive MD data, we

---

[4] Author to whom any correspondence should be addressed.
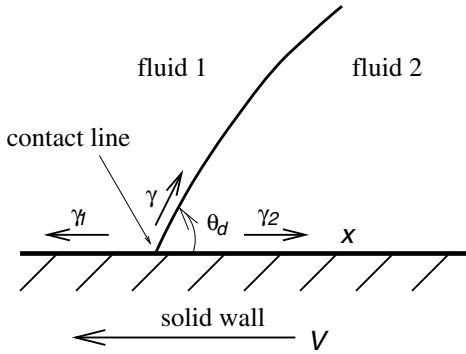
Figure 1. Schematic illustration for immiscible two-phase flows, in which the contact line moves relative to the solid wall. Due to the contact line movement, the dynamic contact angle θ_d deviates from the static contact angle θ_s which is determined by the Young equation $\gamma_1 + \gamma \cos\theta_s = \gamma_2$ (in the partial wetting regime). Here γ_1, γ_2 and γ denote the interfacial tensions for two fluid–solid interfaces and one fluid–fluid interface.

found that the fluid slip measured in nanoscale MD simulations is governed by the generalized Navier boundary condition (GNBC) [21]. The GNBC states that the relative slip velocity between the fluid and the solid wall is proportional to the total tangential stress—the sum of the viscous stress and the uncompensated Young stress; the latter arises from the deviation of the fluid–fluid interface from its static configuration. By combining the GNBC with the Cahn–Hilliard hydrodynamic formulation for immiscible two-phase flows [15, 16, 18, 21], we have obtained a continuum model for MCL hydrodynamics [21]. Its numerical implementation has produced continuum solutions in quantitative agreement with MD simulation results [21, 22]. Recently, it has been shown [23, 24] that the GNBC can be derived in a variational approach based on the Onsager principle of minimum energy dissipation [25, 26].

Textured surfaces with lateral patterns of varying wettability have become technically available recently. There have been experimental and theoretical studies on the morphologies of liquid on surfaces patterned with hydrophilic and hydrophobic regions [27, 28]. While the statics of wetting on patterned surfaces already leads to a large variety of morphologies, the dynamics of spreading and wetting on these surfaces is even more complicated [29–31]. We have applied our continuum model to study the contact line motion on surfaces patterned with stripes of different contact angles [32]. We found that, as the fluid–fluid interface is displaced along the patterned surface, its shape is periodically adjusted by the underlying pattern and the contact line undergoes a stick–slip movement with an oscillatory slip velocity, from which extra dissipation arises inevitably. In this paper we will further demonstrate that the continuum predictions for stick–slip contact line movement can be quantitatively verified by MD simulations. From the oscillatory fluid–fluid interface to the intermittent stick–slip motion of the contact line, we have quantitative agreement between the continuum and MD results. This agreement is attributed to the accurate description by the GNBC down to molecular scale.

This paper is organized as follows. In section 2, there is a brief introduction to the Onsager principle of minimum energy dissipation. The variational approach to MCL hydrodynamics is then presented in section 3. In section 4, the numerical predictions of our continuum hydrodynamic model are compared with MD simulation results for immiscible flows past homogeneous solid surfaces. Section 5 is devoted to the study of contact line motion on chemically patterned surfaces, from model calculations to MD simulations, with remarkable agreement. The paper is concluded in section 6 with a few remarks.

2. The Onsager principle of minimum energy dissipation

First noted by Helmholtz, it is well known that, if the fluid velocity is prescribed at the boundaries, then the solution to the incompressible Stokes equation (with negligible inertia forces) is unique and minimizes the rate of viscous energy dissipation [1]. The variational principles involving energy dissipation (or entropy production) have been further developed by Rayleigh, Onsager and many other people. Below we outline the Onsager principle of minimum energy dissipation that foreshadowed many later developments in statistical mechanics of dissipative systems [25, 26, 33]. As a variational principle, the Onsager principle governs the optimal paths of deviation and restoration to equilibrium. It shall be applied as an approach to the derivation of equations of motion (and, in the present case, boundary conditions as well), in contrast to the principle of minimum free energy which is often used to determine the global state of matter.

We consider a system described by one single variable α measuring the displacement from equilibrium. The overdamped dissipative dynamics is governed by the Langevin equation

$$\eta\dot{\alpha} = -\frac{\partial F(\alpha)}{\partial\alpha} + \varsigma(t), \tag{1}$$

where $\dot{\alpha}$ denotes the rate of change of α, η is the damping coefficient, $F(\alpha)$ is the free energy function and $\varsigma(t)$ is the white noise satisfying the correlation $\langle\varsigma(t)\varsigma(t')\rangle = 2\eta k_B T\delta(t-t')$ with k_B denoting the Boltzmann constant and T the temperature. In equation (1) the dissipative force $-\eta\dot{\alpha}$ is balanced by the conservative force $-\partial F(\alpha)/\partial\alpha$ plus the stochastic force ς. The dynamics of the stochastic variable α may be described by a probability density $P(\alpha, t)$ governed by the Fokker–Planck equation:

$$\frac{\partial P}{\partial t} = D\left[\frac{\partial^2 P}{\partial\alpha^2} + \frac{1}{k_B T}\frac{\partial}{\partial\alpha}\left(\frac{\partial F}{\partial\alpha}P\right)\right], \tag{2}$$

where the diffusion constant D is related to η through the Einstein relation $\eta D = k_B T$. The stationary solution of equation (2) is the equilibrium Boltzmann distribution $P_{eq} \propto \exp[-F(\alpha)/k_B T]$. The corresponding transition probability for α at t to α' at $t + \Delta t$ is given by

$$P(\alpha', t + \Delta t|\alpha, t) = \frac{1}{\sqrt{4\pi D\Delta t}}\exp\left[-\frac{(\alpha'-\alpha)^2}{4D\Delta t}\right]$$

$$\times \exp\left[-\frac{F(\alpha')-F(\alpha)}{2k_B T}\right], \tag{3}$$

for α' close to α and small Δt. By using the Einstein relation, the two exponents can be combined:

$$P(\alpha', t + \Delta t | \alpha, t) = \frac{1}{\sqrt{4\pi D \Delta t}} \exp\left[-\frac{A}{2k_B T}\right], \quad (4)$$

where

$$A = \frac{\eta(\alpha' - \alpha)^2}{2\Delta t} + [F(\alpha') - F(\alpha)] \approx \left[\frac{\eta}{2}\dot{\alpha}^2 + \frac{\partial F(\alpha)}{\partial \alpha}\dot{\alpha}\right]\Delta t \quad (5)$$

is the quantity to be minimized in order to maximize the probability of transition with respect to α'. For small Δt, instead of minimizing A with respect to α', the same is achieved by minimizing with respect to the *rate* $\dot{\alpha} = (\alpha' - \alpha)/\Delta t$. The simple minimization of A yields the equation of force balance:

$$\eta\dot{\alpha} = -\frac{\partial F(\alpha)}{\partial \alpha}, \quad (6)$$

without the stochastic force which has a zero mean.

The above results indicate that (a) there exists a functional, of which the quantity A in equation (5) is the one-variable version, which should be minimized with respect to the rates, (b) such minimization leads to the balance of dissipative and conservative forces on average and (c) the minimization yields the equations of motion and the related boundary conditions, which represent the most probable course of a dissipative process. The last statement guarantees that, statistically, the most probable course will be the only course of action observed in a macroscopic system.

For the general case of multiple variables, the functional for variation is of the form

$$A = \frac{1}{2}\sum_{i,j} \eta_{ij}\dot{\alpha}_i\dot{\alpha}_j + \sum_{i=1}^{n} \frac{\partial F(\alpha_1, \ldots, \alpha_n)}{\partial \alpha_i}\dot{\alpha}_i, \quad (7)$$

where the summation is to be replaced by integrals and partial derivatives by functional derivatives if α_is are field variables. In equation (7) the matrix of damping coefficients η_{ij} must be symmetric due to the microscopic reversibility [25, 26].

3. A variational derivation of moving contact line hydrodynamics

In modeling immiscible two-phase flows, the Cahn–Hilliard free energy functional:

$$F_{CH}[\phi(\mathbf{r})] = \int d\mathbf{r} \left[\frac{K}{2}(\nabla\phi)^2 + \left(-\frac{r}{2}\phi^2 + \frac{u}{4}\phi^4\right)\right], \quad (8)$$

is introduced to stabilize the fluid–fluid interface as a diffuse interface [34]. Here $\phi(\mathbf{r})$ is the field variable (called the phase field) defined as $(\rho_2 - \rho_1)/(\rho_2 + \rho_1)$ with $\rho_{1(2)}$ being the number density of fluid 1 (2) at the spatial point $\mathbf{r}$, and K, r and u are material parameters. The values of K, r and u can be determined from those of the fluid–fluid interfacial thickness $\xi = \sqrt{K/r}$, the interfacial tension $\gamma = 2\sqrt{2}u^2\xi/3r$ and the minima $\phi_{\pm} = \pm\sqrt{r/u}$ of the double-well potential $-r\phi^2/2 + u\phi^4/4$. Among these three quantities, ξ and γ can be measured in equilibrium MD simulations and $\phi_{\pm} = \pm 1$

is set to model the two immiscible fluids (though there is partial miscibility in the narrow interfacial region where ϕ varies between -1 and $+1$). There is also the interfacial free energy per unit area at the fluid–solid interface, $\gamma_{fs}(\phi)$, which changes continuously from the value $\gamma_{fs}(-1)$ (for fluid 1) to $\gamma_{fs}(+1)$ (for fluid 2). We use $\gamma_{fs}(\phi) = (\Delta\gamma_{fs}/2)\sin(\pi\phi/2)$, which is a smooth interpolation from $\gamma_{fs}(-1) = -\Delta\gamma_{fs}/2$ to $\gamma_{fs}(+1) = \Delta\gamma_{fs}/2$. Here $\Delta\gamma_{fs}$ denotes the change of $\gamma_{fs}(\phi)$ from $\phi_{-} = -1$ to $\phi_{+} = +1$, i.e. $\Delta\gamma_{fs} = \gamma_{fs}(\phi_{+}) - \gamma_{fs}(\phi_{-})$. According to the Young equation $\gamma_{fs}(\phi_{-}) = \gamma_{fs}(\phi_{+}) + \gamma\cos\theta_s$, where θ_s is the static contact angle, we have $\Delta\gamma_{fs} = -\gamma\cos\theta_s$ (in the partial wetting regime). The chemical potential μ in the bulk and the similar quantity L at the fluid–solid interface are defined through the variational form of the total free energy:

$$\delta\left\{F_{CH}[\phi] + \int dS\,\gamma_{fs}(\phi)\right\} = \int d\mathbf{r}\,[\mu\delta\phi] + \int dS\,[L\delta\phi], \quad (9)$$

where $\int dS$ denotes the surface integral at the fluid–solid interface and

$$\mu = -K\nabla^2\phi - r\phi + u\phi^3, \quad (10)$$

$$L = K\partial_n\phi + \partial\gamma_{fs}(\phi)/\partial\phi, \quad (11)$$

with n denoting the outward surface normal.

In order to apply the variational principle, we first construct the functional A for minimization with respect to the relevant rates. There are two distinct parts in the functional A in equation (7): the first part is the dissipation function $\Phi = (1/2)\sum_{i,j} \eta_{ij}\dot{\alpha}_i\dot{\alpha}_j$, which is half the rate of dissipation, being positive definite and quadratic in the rates $\dot{\alpha}_i$s; the second is the rate of change of the free energy $\dot{F} = \sum_{i=1}^{n}(\partial F/\partial\alpha_i)\dot{\alpha}_i$.

Physically, there are four sources of dissipation: the bulk viscous dissipation, the dissipation due to diffusion in the fluid–fluid interfacial region, the frictional dissipation at the fluid–solid interface and the relaxational dissipation around the contact line. The rate of bulk viscous dissipation is of the standard form

$$R_v = \int d\mathbf{r}\left[\frac{\eta}{2}(\partial_i v_j + \partial_j v_i)^2\right], \quad (12)$$

where η is the shear viscosity in the bulk fluid. Regarding the fluid and solid similarly as collections of molecules but with different interactions, we assume that the form of the energy dissipation at the fluid–solid interface is similar to that of the bulk viscous dissipation. It follows that the rate of the frictional dissipation at the fluid–solid interface is of the form

$$R_s = \int dS\,[\beta(v_\tau^{slip})^2], \quad (13)$$

where v_τ^{slip} is the slip velocity, defined as the relative velocity in the tangential (τ) direction between the fluid and the solid at the fluid–solid interface, and β is the slip coefficient which has the dimension of [viscosity]/[length]. Hence a slip length may be defined as $l_s = \eta/\beta$ [35]. (The no-slip boundary condition corresponds to the limit of infinite slip coefficient β.) It is worth emphasizing that, while R_{slip} arises from

the assumption of relative slip at the fluid–solid interface, there is no specification of how much slippage there should be. Even an infinitesimal slippage would lead to the form in equation (13). Note that in both equations (12) and (13) the rate variables (i.e. $\dot\alpha_i$s in equation (7)) are the fluid velocities.

For small perturbations away from the two-phase equilibrium ($\mu = \text{const.}$ and $L = 0$), there are dissipations due to diffusion and relaxation. Here the relevant variable is ϕ, the relative concentration of the two fluid species. As a conserved parameter, ϕ satisfies the continuity equation

$$\dot\phi = \frac{\partial\phi}{\partial t} + \mathbf{v}\cdot\nabla\phi = -\nabla\cdot\mathbf{J}, \qquad (14)$$

where $\mathbf{J}$ is the diffusive current density which is the rate variable here. Since the rate of dissipation must be quadratic in rate variables, we propose

$$R_{\mathrm{d}} = \int \mathrm{d}\mathbf{r}\left[\frac{\mathbf{J}^2}{M}\right], \qquad (15)$$

for the form of diffusive dissipation, where M is the mobility coefficient. At the fluid–solid interface, ϕ is no longer conserved because diffusive transport normal to the solid surface is allowed ($\partial_n J_n \neq 0$ in general). The rate variable here is $\dot\phi$ and correspondingly the rate of relaxational dissipation is

$$R_{\mathrm{r}} = \int \mathrm{d}S\left[\frac{\dot\phi^2}{\Gamma}\right], \qquad (16)$$

where Γ is a positive constant.

For the rate of change of the free energy $\dot F$, we replace $\delta\phi$ by $\partial\phi/\partial t = \dot\phi - \mathbf{v}\cdot\nabla\phi$ in equation (9) and obtain

$$
\begin{aligned}
\dot F &= \int \mathrm{d}\mathbf{r}\left[\mu\frac{\partial\phi}{\partial t}\right] + \int \mathrm{d}S\left[L\frac{\partial\phi}{\partial t}\right] = \int \mathrm{d}\mathbf{r}\,[\mu(\dot\phi - \mathbf{v}\cdot\nabla\phi)]\\
&\quad + \int \mathrm{d}S\,[L(\dot\phi - \mathbf{v}\cdot\nabla\phi)] = \int \mathrm{d}\mathbf{r}\,[-\mu\nabla\cdot\mathbf{J} - \mu\mathbf{v}\cdot\nabla\phi]\\
&\quad + \int \mathrm{d}S\,[L\dot\phi - Lv_\tau\partial_\tau\phi] = \int \mathrm{d}\mathbf{r}\,[\nabla\mu\cdot\mathbf{J} - \mu\mathbf{v}\cdot\nabla\phi]\\
&\quad + \int \mathrm{d}S\,[L\dot\phi - Lv_\tau\partial_\tau\phi]
\end{aligned}
\qquad (17)
$$

where $\dot\phi$ is replaced by $-\nabla\cdot\mathbf{J}$ according to the continuity equation and integration by parts is used with $\int \mathrm{d}\mathbf{r}\,[\nabla\cdot(\mu\mathbf{J})] = \int \mathrm{d}S\,[\mu J_n] = 0$ from $J_n = 0$ at the solid surface. Physically, the last line of equation (17) may be decomposed into the entropy part and the work part, i.e. $\dot F = -T\dot S - \dot W$, where

$$T\dot S = \int \mathrm{d}\mathbf{r}\,[-\nabla\mu\cdot\mathbf{J}] + \int \mathrm{d}S\,[-L\dot\phi], \qquad (18)$$

and

$$\dot W = \int \mathrm{d}\mathbf{r}\,[\mathbf{v}\cdot(\mu\nabla\phi)] + \int \mathrm{d}S\,[v_\tau(L\partial_\tau\phi)]. \qquad (19)$$

While the entropy part $T\dot S$ comes from the diffusion and boundary relaxation of the relative concentration ϕ, the work part ($\dot W$ for the work done by the interface to the flow) shows the 'elastic' force and stress exerted by the interface on the

flow. Here $\mu\nabla\phi$ is the capillary force density and $L\partial_\tau\phi$ is the (tangential) Young stress due to the fluid–fluid interface.

Now we write the functional $A = (R_{\mathrm{v}} + R_{\mathrm{s}} + R_{\mathrm{d}} + R_{\mathrm{r}})/2 + \dot F$ as

$$
\begin{aligned}
A[\mathbf{v}(\mathbf{r}), \mathbf{J}(\mathbf{r}), \dot\phi(\mathbf{r})] &= \int \mathrm{d}\mathbf{r}\left[\frac{\eta}{4}(\partial_i v_j + \partial_j v_i)^2\right]\\
&\quad + \int \mathrm{d}S\left[\frac{\beta}{2}(v_\tau^{\mathrm{slip}})^2\right] + \int \mathrm{d}\mathbf{r}\left[\frac{\mathbf{J}^2}{2M}\right] + \int \mathrm{d}S\left[\frac{\dot\phi^2}{2\Gamma}\right]\\
&\quad + \int \mathrm{d}\mathbf{r}\,[\nabla\mu\cdot\mathbf{J}] + \int \mathrm{d}S\,[L\dot\phi] + \int \mathrm{d}\mathbf{r}\,[-\mathbf{v}\cdot(\mu\nabla\phi)]\\
&\quad + \int \mathrm{d}S\,[-v_\tau(L\partial_\tau\phi)]
\end{aligned}
\qquad (20)
$$

which is to be minimized with respect to the three rates $\{\mathbf{v}, \mathbf{J}, \dot\phi\}$, supplemented with the incompressibility condition $\nabla\cdot\mathbf{v} = 0$. Minimizing A with respect to $\mathbf{J}$ involves only two terms in equation (20) and gives the constitutive relation

$$\mathbf{J} = -M\nabla\mu. \qquad (21)$$

Substituting equation (21) into the continuity equation (14) leads to the convection–diffusion equation

$$\frac{\partial\phi}{\partial t} + \mathbf{v}\cdot\nabla\phi = M\nabla^2\mu. \qquad (22)$$

Similar minimization with respect to $\dot\phi$ at the solid surface leads to the boundary condition for relaxation of ϕ:

$$\frac{\partial\phi}{\partial t} + v_\tau\partial_\tau\phi = -\Gamma L. \qquad (23)$$

For minimization with respect to $\mathbf{v}$, it is necessary to impose the incompressibility condition $\nabla\cdot\mathbf{v} = 0$ by the use of a Lagrange multiplier $\lambda(\mathbf{r})$ which leads to an extra term $\int \mathrm{d}\mathbf{r}\,[\lambda\nabla\cdot\mathbf{v}]$. Then, minimizing A with respect to the fluid velocity results in a group of volume integrals:

$$
\begin{aligned}
&-\eta\int \mathrm{d}\mathbf{r}\,[\partial_j(\partial_j v_i + \partial_i v_j)\delta v_i] - \int \mathrm{d}\mathbf{r}\,[\mu\partial_i\phi\delta v_i]\\
&\quad - \int \mathrm{d}\mathbf{r}\,[\partial_i\lambda\delta v_i] = 0,
\end{aligned}
\qquad (24)
$$

from which we obtain the Stokes equation:

$$-\nabla p + \eta\nabla^2\mathbf{v} + \mu\nabla\phi = 0, \qquad (25)$$

where the Lagrange multiplier appears through the pressure $p = -\lambda$. In the presence of inertial forces, the Stokes equation is immediately generalized to the Navier–Stokes equation:

$$\rho_{\mathrm{m}}\left[\frac{\partial\mathbf{v}}{\partial t} + \mathbf{v}\cdot\nabla\mathbf{v}\right] = -\nabla p + \eta\nabla^2\mathbf{v} + \mu\nabla\phi, \qquad (26)$$

where ρ_{m} is the mass density. Minimizing A with respect to the (tangential) velocity at the fluid–solid interface results in a group of surface integrals

$$
\begin{aligned}
&\eta\int \mathrm{d}S\,[\partial_n v_\tau\delta v_\tau + \partial_\tau v_n\delta v_\tau] + \beta\int \mathrm{d}S\,[v_\tau^{\mathrm{slip}}\delta v_\tau]\\
&\quad - \int \mathrm{d}S\,[L\partial_\tau\phi\delta v_\tau] = 0,
\end{aligned}
\qquad (27)
$$

from which the slip boundary condition is obtained in the form of

$$\beta v_\tau^{\text{slip}} = -\eta(\partial_n v_\tau + \partial_\tau v_n) + L\partial_\tau \phi. \qquad (28)$$

As the slip coefficient at the fluid–solid interface, β can be different for the two fluid species. We use $\beta = \beta(\phi)$ which is a function of local relative concentration. From our derivation it is clear that equations (23) and (28), denoted the generalized Navier boundary conditions, constitute a consistent pair because they emerge consistently from the principle of minimum energy dissipation. It is important to note that $L = 0$ at equilibrium and the uncompensated Young stress $L\partial_\tau \phi$ in equation (28) satisfies

$$\int_{\text{int}} d\tau \, [L\partial_\tau \phi] = \gamma(\cos\theta_d - \cos\theta_s), \qquad (29)$$

in the sharp interface limit [36]. Here $\int_{\text{int}} d\tau$ denotes the integration across the fluid–fluid interface along the tangential direction and θ_d is the dynamic contact angle. Equation (29) indicates that the uncompensated Young stress arises from the deviation of the fluid–fluid interface from its static configuration. The contact line motion is determined by equations (22), (23), (26) and (28), supplemented by the incompressibility condition $\nabla \cdot \mathbf{v} = 0$ and the impermeability conditions $v_n = 0$ and $\partial_n \mu = 0$ at the solid surface. It is interesting to point out that, with noise terms added to equations (22) and (26) in the bulk, the CH hydrodynamic formulation has long been used to study the critical dynamics in binary fluids, commonly referred to as Model H [37].

## 4. Comparison of MD and continuum hydrodynamics results

MD simulations have been performed for immiscible two-phase Couette and Poiseuille flows [21–23]. The two immiscible fluids were confined between two planar solid walls parallel to the xy plane, with the fluid–solid interfaces defined at $z = 0$ and H. Interaction between the fluid molecules was modeled by a modified Lennard-Jones potential $U_{\text{ff}} = 4\varepsilon[(\sigma/r)^{12} - \delta_{\text{ff}}(\sigma/r)^6]$, where r is the distance between the molecules, ε and σ are the energy and length scales of the interaction, respectively, and $\delta_{\text{ff}} = 1$ for like molecules and $\delta_{\text{ff}} = -1$ for molecules of different species. Each solid wall was constructed by two [001] planes of an fcc lattice, with each wall molecule attached to a lattice site by a harmonic spring. The mean square displacement of wall molecules was controlled to obey the Lindemann criterion. The fluid–solid interaction was modeled by another modified Lennard-Jones potential $U_{\text{fs}} = 4\varepsilon_{\text{fs}}[(\sigma_{\text{fs}}/r)^{12} - \delta_{\text{fs}}(\sigma_{\text{fs}}/r)^6]$, with the energy and range parameters $\varepsilon_{\text{fs}} = 1.16\varepsilon$ and $\sigma_{\text{fs}} = 1.04\sigma$, and the parameter δ_{fs} for tuning the wetting property of the fluid. The interaction potentials U_{ff} and U_{fs} were both cut off at $r_c = 2.5\sigma$. The mass of the wall molecule was set equal to that of the fluid molecule m, and the average number densities for the fluids and wall were set at $\rho = 0.81\sigma^{-3}$ and $\rho_w = 1.86\sigma^{-3}$, respectively. The temperature was controlled at $2.8\varepsilon/k_B$, where k_B is the Boltzmann constant. This high temperature was used to suppress the fluid density oscillation along the

surface normal near the solid surface, for a better comparison with the continuum model calculations (for uniform densities). To maintain constant temperature, damping and a Langevin noise were added to the equations for the y component of the velocity. Since the y direction is perpendicular to the plane of two-dimensional hydrodynamics (i.e. the xz plane), this does not bias the flow fields. To induce the Couette flow, the top and bottom walls were moved at a constant speed V in the $\pm x$ directions, respectively. Applying an external force $mg\hat{\mathbf{x}}$ on each fluid molecule induced the Poiseuille flow. Periodic boundary conditions were imposed on the x and y boundaries of the sample. Two different cases were considered in our simulations. The symmetric case refers to identical fluid–solid interactions for the two fluids (both of $\delta_{\text{fs}} = 1$), with a 90° static contact angle. The asymmetric case refers to different fluid–solid interactions, with $\delta_{\text{fs}} = 1$ for one and $\delta_{\text{fs}} = 0.7$ for the other. The simulated fluids measured 6.8σ to 68σ between the solid walls (for H in the z direction) and 6.8σ in the y direction. The extension in the x direction was long enough, typically about five times H, to allow the stationary single-phase velocity field to appear in regions far away from the fluid–fluid interface (see the following figures).

To demonstrate the validity of our continuum model presented in section 3, we have obtained numerical solutions that can be directly compared with the MD results for fluid velocity and fluid–fluid interface. The Navier–Stokes equation was solved using a pressure–Poisson solver [21] and a semi-implicit scheme was employed to solve the fourth-order diffusion equation for large systems. A detailed finite difference scheme can be found in [21]. We have carried out the MD–continuum comparison in such a way that virtually no adjustable parameter is involved in the continuum calculations. The details and parameter values can be found in [21] and [22]. We want to emphasize that here the (macroscopic) continuum model was solved for those nanoscopic systems in our MD simulations. All the material parameters and length and timescales in the continuum calculations were measured or taken from MD simulations. The continuum solutions were then compared with MD results directly. The direct MD–continuum comparison involves no scaling between microscopic (MD) and macroscopic (continuum) scales of length and time. No free parameter was introduced into such a comparison since our purpose here was to demonstrate the validity of the model. Below we show the remarkable overall agreement through a few examples. We want to point out that the MD results in figures 2–5 were obtained for stationary states in which the time average can be performed in arbitrarily long time intervals to reduce the statistical fluctuations.
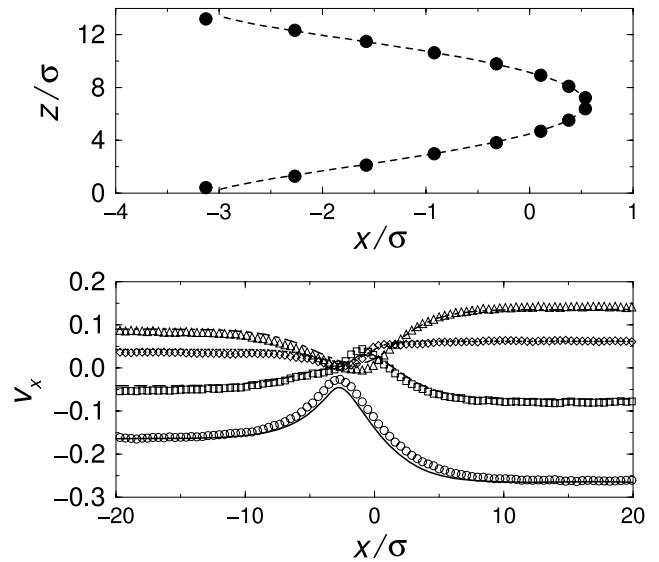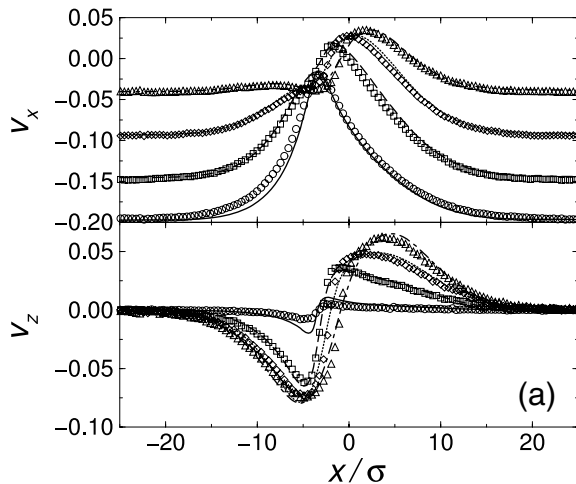
Figure 2 shows the MD and continuum fluid–fluid interface profiles for two immiscible Couette flows. The corresponding MD and continuum velocity fields are shown in figure 3. In order to further verify that the continuum model is local and the parameter values are local properties, and hence applicable to different flow geometries, the MD–continuum comparison is also presented for an immiscible Poiseuille flow in figure 4.

Another important MD–continuum comparison is the interpolation behavior between the near-complete slip at the
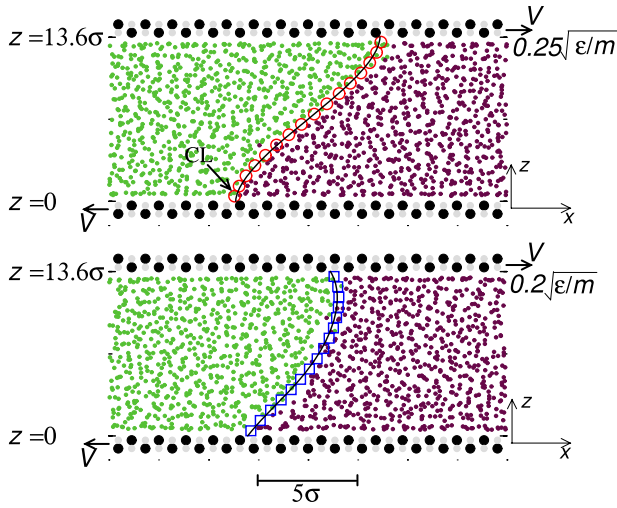
Figure 2. Segments of the MD simulations for immiscible Couette flows. The colored dots denote the instantaneous molecular positions of the two fluids projected onto the *xz* plane. The black and gray circles denote the wall molecules. The upper panel illustrates the symmetric case of $V = 0.25\sqrt{\varepsilon/m}$ and $H = 13.6\sigma$; the lower panel illustrates the asymmetric case of $V = 0.2\sqrt{\varepsilon/m}$ and $H = 13.6\sigma$. The red circles and blue squares represent the time-averaged fluid–fluid interface profiles, defined at $\rho_1 = \rho_2$ ($\phi = 0$). The black solid lines are the interface profiles calculated from the continuum model.


Figure 4. Comparison of the MD (symbols) and continuum (lines) results for an asymmetric immiscible Poiseuille flow. An external force $mg = 0.05\varepsilon/\sigma$ is applied on each fluid molecule in the $+x$ direction, and the two walls separated by $H = 13.6\sigma$ move at a constant speed $0.51\sqrt{\varepsilon/m}$ in the $-x$ direction to maintain a stationary fluid–fluid interface. (a) Fluid–fluid interface. (b) $v_x(x)$ at different z levels. The profiles are symmetric about the plane of $z = H/2$, hence only the lower half is shown at $z = 0.425\sigma$ (circles and solid line), 2.125σ (squares and dashed line), 3.825σ (diamonds and dotted line) and 5.525σ (triangles and dotted–dashed line).

MCL (see figures 3 and 4) and the small amount of partial slip far away from the contact line (for $l_s = \eta/\beta \ll H$). MD simulations have been carried out for immiscible Couette flows in increasingly wider channels [22]. The inset to figure 5 shows the variation of tangential velocity at the wall. Immediately next to the MCL, there is a small core region characterized by a sharp decay of slip. As the channel width H increases, a much more gentle variation of the slip profiles shows up. In

order to reveal the nature of this slow variation, we plot in figure 5 the same data in the log–log scale. The dashed line has a slope -1, indicating the $1/x$ behavior of the slip profile, where x is the distance away from the MCL. The plateau in each single-phase flow region is formed at the constant amount of slip $v_0^{\text{slip}} = 2Vl_s/(H + 2l_s)$ due to the finite H. Obviously,
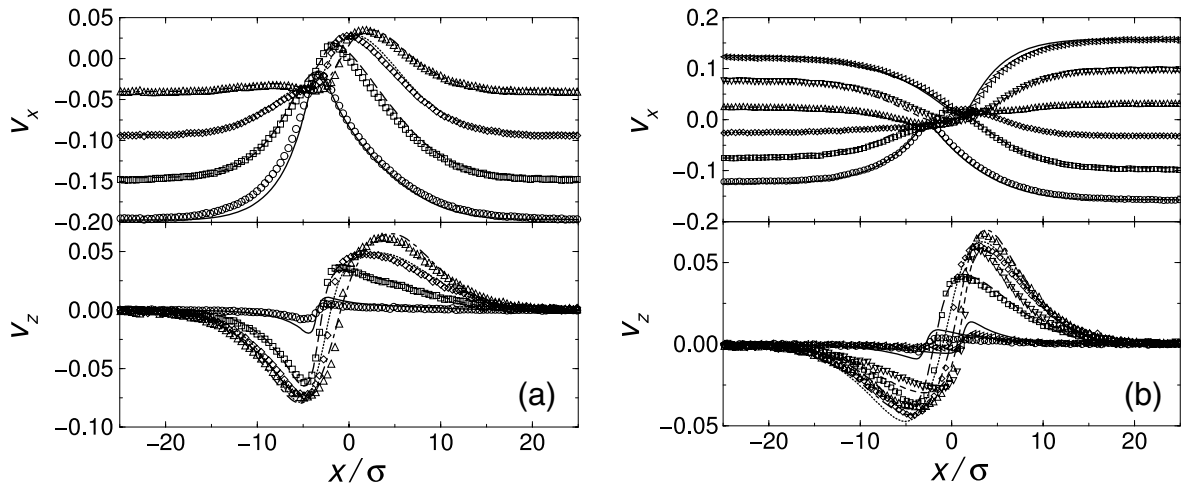
Figure 3. Comparison of the MD (symbols) and continuum (lines) velocity profiles ($v_x(x)$ and $v_x(x)$ at different z levels). (a) The symmetric case in figure 2. The profiles are symmetric about the plane of $z = H/2$, hence only the lower half is shown at $z = 0.425\sigma$ (circles and solid lines), 2.125σ (squares and dashed lines), 3.825σ (diamonds and dotted lines) and 5.525σ (triangles and dotted–dashed lines). (b) The asymmetric case in figure 2, shown at $z = 0.425\sigma$ (circles and solid lines), 2.975σ (squares and long-dashed lines), 5.525σ (diamonds and dotted lines), 8.075σ (up-triangles and dotted–dashed lines), 10.625σ (down-triangles and dashed lines) and 13.175σ (left-triangles and solid lines). Although the solid lines are used to denote two different z levels in (b), for each solid line, whether it should be compared to circles or left-triangles is self-evident.
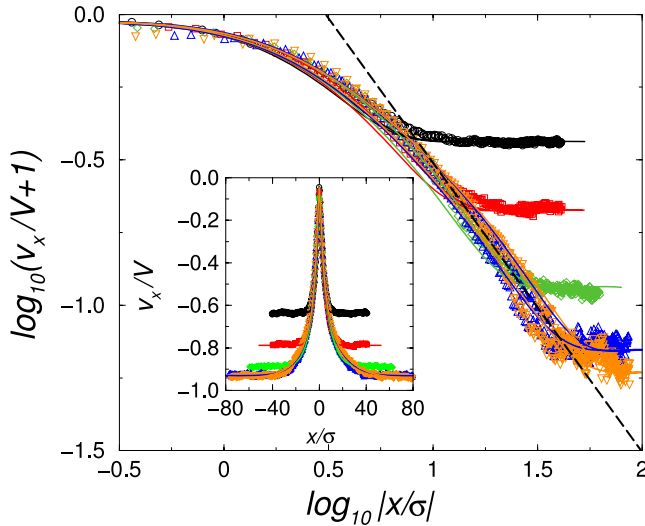
Figure 5. Log–log plot for the slip profiles. Here $v_x/V + 1$ is the scaled slip velocity at $z = 0$ (relative to the wall moving at $-V\hat{x}$) and x/σ measures the distance from the MCL. The $v_x(x)$ profiles were obtained for five symmetric Couette flows, with different values for H but the same value $0.05\sqrt{\varepsilon/m}$ for V. The MD (symbols) and continuum (lines) results are shown for $H = 6.8\sigma$ (black circles and line), 13.6σ (red squares and line), 27.2σ (green diamonds and line), 54.4σ (blue up-triangles and line) and 68σ (orange down-triangles and line). There are two lines for each color, one for the slip profile to the left of the MCL and the other to the right of the MCL. The dashed line has a slope of -1, indicating that the $1/x$ behavior is approached for increasingly large H. Inset: the scaled tangential velocity v_x/V at $z = 0$, plotted as a function of x/σ.

as $H/l_s \to \infty$ and $v_0^{\text{slip}}/V \to 0$ (no slip), the power-law region becomes very wide. This large $1/x$ partial-slip region indicates that the outer cutoff length scale (e.g. the system dimension) would determine the integrated effects, such as the total dissipation. In fact, the $1/x$ stress variation away from the MCL has been known for decades [2]. However, to our knowledge the fact that the partial slip also exhibits the same spatial dependence was first presented in [22].

It is worth emphasizing that the MD–continuum agreement has been achieved from the molecular scale vicinity of the MCL to regions far away from the MCL. We want to point out that the continuum model is local and the material parameter values are local properties, applicable to different flow geometries and different system sizes. That is, the same set of model parameters (corresponding to the same local properties in a series of MD simulations) has been used to calculate velocity fields and fluid–fluid interface shapes for comparison with MD results obtained for different external conditions (e.g. V, H and flow geometry). The overall agreement is excellent, demonstrating the validity of the generalized Navier boundary conditions and the hydrodynamic model.

5. Stick–slip motion of moving contact line on chemically patterned surfaces

Our continuum model has also been used to study the contact line motion on chemically patterned surfaces [32]. We
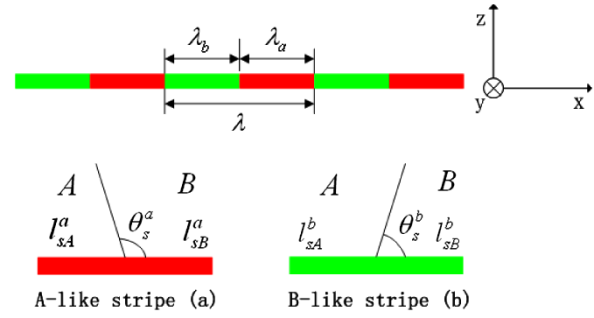
Figure 6. Schematic illustration for the chemically patterned surface with alternating A-like and B-like stripes. Each stripe is characterized by a static contact angle and two slip lengths. The A-like and B-like stripes are of widths λ_a and λ_b and the pattern period is $\lambda = \lambda_a + \lambda_b$.

considered an immiscible two-phase fluid flowing past surfaces patterned with stripes of different contact angles We found that the shape of the fluid–fluid interface is periodically adjusted by the underlying pattern and the contact line undergoes a stick–slip movement with the slip velocity oscillating in both space and time. The purpose of this section is to demonstrate that the continuum predictions for stick–slip contact line movement can be quantitatively verified by MD simulations. From the oscillatory fluid–fluid interface to the intermittent stick–slip motion of the contact line, we have obtained quantitative agreement between the continuum and MD results. This agreement is attributed to the accurate description by the generalized Navier boundary conditions down to molecular scale.

5.1. Modeling chemically patterned surfaces

We consider immiscible two-phase flows through a two-dimensional channel (a slit pore) in which the top surface is homogeneous (labeled by c) while the bottom surface is chemically patterned. There are two immiscible phases A and B in the two-phase fluid. The bottom surface is patterned by the A-like and B-like stripes, labeled by a and b, respectively. The A phase is more attracted to the A-like stripe while the B phase is more attracted to the B-like stripe, as illustrated in figure 6. The properties of each stripe can be specified by a static contact angle (defined on the side of fluid phase B): θ_s^a at the A-like stripe (a) or θ_s^b at the B-like stripe (b), and two slip lengths: l_{sA}^a and l_{sB}^a at the A-like stripe or l_{sA}^b and l_{sB}^b at the B-like stripe for the two phases. To reduce the number of independent parameters, we assume $\theta_s^b = 180° - \theta_s^a$ (with $\theta_s^b < 90°$), $l_{sA}^a = l_{sB}^b$ and $l_{sA}^b = l_{sB}^a$. Since larger slip length is associated with a less attractive fluid–solid interaction [38], we use $l_{sA}^a < l_{sA}^b$.

In the present continuum modeling of inhomogeneous surfaces, the static contact angle and slip lengths appear as locally defined material parameters. For the patterned surfaces shown in figure 6, each of these parameters varies as a step function across the stripe boundary. In the study of single-phase flows past chemically patterned surfaces [39–42], we have shown through both MD and continuum simulations that the slip length can be locally defined for a continuum
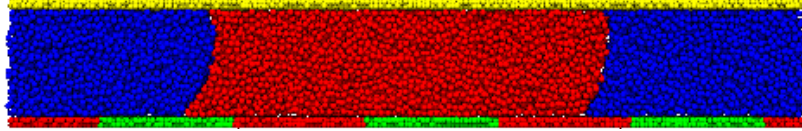
Figure 7. MD simulation sample for the immiscible Poiseuille flows. The colored symbols indicate the instantaneous molecular positions projected onto the xz plane. Here the fluid A is blue, the fluid B is red, the solid a is red, the solid b is green and the solid c is yellow. The fluid B appears to be sandwiched by the fluid A due to the periodic boundary condition along the x direction. For the static contact angle $\theta_s^a (>90°)$, we note that the fluid B is left to the fluid A on the A-like stripe here whereas in figure 6, B is to the right of A. We collect the data for the interface with B to the right of A.

Table 1. Parameters measured from MD simulations for continuum hydrodynamic calculations. We use $\delta_{Aa} > \delta_{Ba} > 0$ and $\delta_{Bb} > \delta_{Ab} > 0$ to ensure that the fluid A is more attracted to the A-like stripe and the fluid B is more attracted to the B-like stripe. We also assume $\delta_{Aa} = \delta_{Bb}$ and $\delta_{Ab} = \delta_{Ba}$ to reduce the number of independent parameters. Consequently, we have $\theta_s^b < 90°$, $\theta_s^a = 180° - \theta_s^b$ and $l_{sA}^a = l_{sB}^b < l_{sA}^b = l_{sB}^a$ for the patterned surface. As for the homogeneous surface, we have $\delta_{Ac} = \delta_{Bc}$, hence $\theta_s^c = 90°$ for the static contact angle and $l_{sA}^c = l_{sB}^c$ for the two slip lengths.

Parameters for MD simulations	Parameters for continuum calculations
$\delta_{Aa} = 0.7, \delta_{Ab} = 0.2, \delta_{Ac} = 0.7$	$\theta_s^b \approx 57°, l_{sA}^a \approx 1.9\sigma, l_{sA}^b \approx 14.3\sigma, l_{sA}^c \approx 1.9\sigma$
$\delta_{Aa} = 0.8, \delta_{Ab} = 0.2, \delta_{Ac} = 0.8$	$\theta_s^b \approx 47°, l_{sA}^a \approx 1.2\sigma, l_{sA}^b \approx 14.3\sigma, l_{sA}^c \approx 1.2\sigma$
$\delta_{Aa} = 0.7, \delta_{Ab} = 0.3, \delta_{Ac} = 0.5$	$\theta_s^b \approx 66°, l_{sA}^a \approx 1.9\sigma, l_{sA}^b \approx 10.3\sigma, l_{sA}^c \approx 4.6\sigma$

hydrodynamic description as long as the fluid–solid interaction does not change too fast compared to the pattern period [42]. Physically, a continuum hydrodynamic model describes those variations that are slow in both space and time and the parameters involved in such a model can be locally defined in a coarse-grained sense.

5.2. Molecular dynamics simulations

MD simulations have been performed for two immiscible fluids that are confined in a slit pore by two planar solid walls parallel to the xy plane (see figure 7). The top wall has a homogeneous surface at $z = H$ and the bottom wall has a patterned surface at $z = 0$. The top wall is labeled by c, and the two fluids are labeled by A and B, respectively. The bottom wall is periodically patterned with A-like and B-like stripes, which are labeled by a and b, respectively, and are of widths λ_a and λ_b, as already set in the continuum model. The extension of the MD simulation box in the x direction is set as an integral multiple of the pattern period $\lambda = \lambda_a + \lambda_b$, typically two to five times λ. The values of H and λ will be given in section 5.4 where the simulation results are presented.

In our MD simulations, interaction between any two molecules separated by a distance r is modeled by a modified Lennard-Jones potential $U_{\alpha\beta} = 4\varepsilon_{\alpha\beta}[(\sigma_{\alpha\beta}/r)^{12} - \delta_{\alpha\beta}(\sigma_{\alpha\beta}/r)^6]$, where the subscripts α and β denote the molecule species A, B, a, b and c. The energy parameters $\varepsilon_{\alpha\beta}$ and the range parameters $\sigma_{\alpha\beta}$ for fluid–fluid interactions are given by ε and σ, respectively, while those for fluid–solid interactions are given by 1.16ε and 1.04σ, respectively. The dimensionless parameter $\delta_{\alpha\beta}$ is used to ensure the immiscibility between the two fluids and to tune the wetting property of each fluid as well. We use $\delta_{AA} = \delta_{BB} = 1$ and $\delta_{AB} = \delta_{BA} = -1$ to ensure the immiscibility, and $\delta_{Aa} > \delta_{Ba} > 0$ and $\delta_{Bb} > \delta_{Ab} > 0$ for fluid–solid interactions, which ensure that the fluid A is more attracted to the A-like stripe while the fluid

B is more attracted to the B-like stripe. To reduce the number of independent parameters, we further assume $\delta_{Aa} = \delta_{Bb}$ and $\delta_{Ab} = \delta_{Ba}$. The two fluids have the same interaction with the top wall, hence $\delta_{Ac} = \delta_{Bc}$. The mass of each fluid molecule and that of each wall molecule are both m. The average number density of fluid molecules is $\rho = 0.81\sigma^{-3}$ while the number density of wall molecules is $\rho_w = 1.86\sigma^{-3}$. The temperature is controlled at $1.4\varepsilon/k_B$ by the Langevin thermostat. This temperature is lower than that used in section 4 because weak thermal fluctuations are desired considering the difficulty in obtaining clean data from transient states. The equations of motion are integrated using the velocity Verlet algorithm with a time step $\Delta t = 0.001\tau$, where $\tau = \sqrt{m\sigma^2/\varepsilon}$. The interaction potential $U_{\alpha\beta}$ is cut off at $r_c = 2.5\sigma$. Periodic boundary conditions are imposed in the x and y directions.

To drive the immiscible two-phase Poiseuille flows, a body force $mg\hat{x}$ is applied to each fluid molecule. In our simulations, the two fluids are always separated by a clear interface while flowing past the patterned surface. In both the static and dynamic states, the average molecular densities ρ_1 and ρ_2 for the two fluids are measured to locate the interface (by the condition $\rho_1 = \rho_2$, i.e. $\phi = 0$). From the time evolution of the interface, the contact line velocity is calculated by differentiating the contact line position with respect to time.

As stated in section 5.1, the properties of each solid surface (a, b or c), physically determined by the corresponding fluid–solid interactions, can be specified by two slip lengths (for the two fluids A and B) and a static contact angle (defined on the side of fluid B). Given the fluid–solid interaction for one fluid at one solid surface, the slip length can be measured from non-equilibrium MD simulations in single-phase Couette-flow geometry [38]. Given the fluid–solid interactions for two fluids at one solid surface, the static contact angle can be measured from equilibrium MD simulations. Results from these measurements are listed in table 1. The shear viscosity $\eta = 2.0\sqrt{\varepsilon m}/\sigma^2$ and the fluid–fluid interfacial tension

$\gamma = 4.75\varepsilon/\sigma^2$ are also measured for the continuum model
Once the number density and the temperature are specified
for a Lennard-Jones fluid, non-equilibrium simulations can be
carried out for Couette flows, in which the shear stress and
the shear rate are measured, from which the shear viscosity
η is computed. As to the interfacial tension γ, equilibrium
simulations can be carried out for two immiscible fluids with
an interface stabilized in between, and γ is computed by
integrating the magnitude of the stress anisotropy measured in
the interfacial region.

5.3. Continuum hydrodynamic calculations and comparison with MD simulations

For continuum calculations, we have measured in MD
simulations the number density ρ, the shear viscosity η, the
interfacial tension γ, the interfacial thickness $\xi \cong 0.3\sigma$, the
static contact angle θ_s^b and the slip lengths l_{sA}^a, l_{sA}^b and l_{sA}^c. As
for the two phenomenological parameters M and Γ, we use
$M = 0.023\sigma^4/\sqrt{m\varepsilon}$ and $\Gamma = 0.66\sigma/\sqrt{m\varepsilon}$, optimized values
for earlier comparison of continuum and MD results [21–23].
The two fluid phases may have different interactions with the
solid, and hence the slip coefficient β may vary with ϕ at the
surface. At each stripe (a or b), we use $\beta(\phi) = (1-\phi)\beta_1/2 +
(1+\phi)\beta_2/2$ with ϕ varying between -1 and $+1$ across the
fluid–fluid interface and β varying between $\beta(-1) = \beta_1$ and
$\beta(+1) = \beta_2$ accordingly.

Continuum calculations are carried out for immiscible
two-phase flows through a slit pore with homogeneous top
surface and patterned bottom surface. The flow is driven by
an external force density $\mathbf{f}_e = \rho mg\hat{\mathbf{x}}$ along the x direction, for
direct comparison with MD simulations in which an external
force $mg\hat{\mathbf{x}}$ is applied to each fluid molecule. Appropriate
velocity boundary conditions are applied at the left and right
boundaries of the channel in the computational domain, given
by the Poiseuille-type quadratic profile $\mathbf{v}(z) = v_x(z)\hat{\mathbf{x}}$ which
satisfies $\eta\partial_z^2 v_x + \rho mg = 0$ and the slip boundary conditions at
the top and bottom surfaces. We use a pressure–Poisson solver
for the Navier–Stokes equation and a semi-implicit scheme for
the diffusion equation [21, 22]. For direct comparison with
the MD results, the continuum results will be presented in the
reduced units defined by the Lennard-Jones energy scale ε,
length scale σ and molecular mass m.

For contact line motion on patterned surfaces, the
comparison of continuum and MD results can no longer
be made for stationary states in which the continuum
hydrodynamic variables, e.g. ϕ and $\mathbf{v}$, are time-independent
(see section 4). Instead, the stick–slip movement of
the contact line requires such a comparison to be done
for transient states in which the fluid–fluid interface takes
oscillatory shape while the contact line moves at oscillatory
velocity. Technically, in order to resolve the time evolution
in continuum hydrodynamics, the time averaging in MD
simulations has to be performed within time intervals that are
short enough compared to the characteristic timescales shown
in the continuum solutions. To further remove the statistical
fluctuations, we also average the velocity and density variables
over an ensemble of similar systems, generated by a series of
simulations consistent with all the 'macroscopic' restraints.
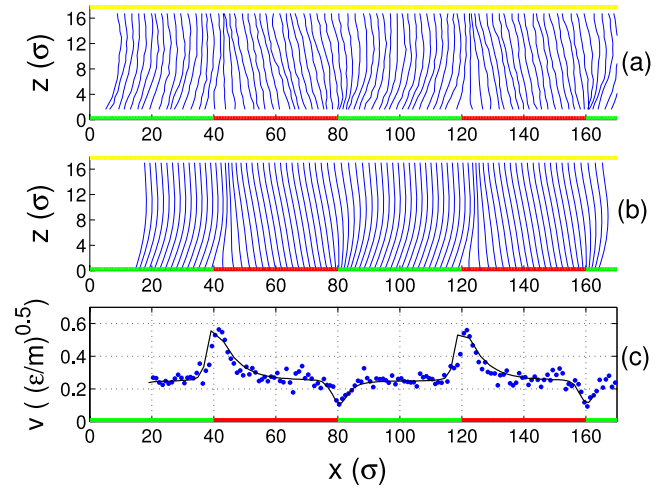
Figure 8. (a) Moving fluid–fluid interface in MD simulation. The
time interval between two adjacent interfaces is 8τ. (b) Moving
fluid–fluid interface in continuum calculation. The time interval
between two adjacent interfaces is 7τ. (c) Contact line velocity at the
lower patterned surface, plotted as a function of the contact line
position, with symbols for MD results and line for continuum results.
The parameters used for interaction potentials are
$\delta_{Aa} = \delta_{Bb} = \delta_{Ac} = \delta_{Bc} = 0.7$ and $\delta_{Ab} = \delta_{Ba} = 0.2$. The external
force on each fluid molecule is $mg = 0.015\varepsilon/\sigma$. The distance
between the bottom and top walls is $H = 17\sigma$. The pattern period is
$\lambda = 80\sigma$ with $\lambda_a = \lambda_b$.

5.4. Numerical results

In order to let the relaxation of the fluid–fluid interface be
fully manifested, we start from patterned surfaces of large
period. Figure 8 shows the variations of fluid–fluid interface
and contact line velocity along the patterned surface (at the
bottom of the channel). It is observed that the fluid–fluid
interface is displaced with constant shape and velocity when
it is away from the boundaries between different stripes. Close
to each of these boundaries, however, there is a fast variation
in contact line velocity, either a sharp increase followed by a
gentle decrease or a sharp decrease followed by an increase.
That is, the contact line is forced into an intermittent stick–slip
motion by the patterned surface. It is readily seen that the fast
variation of contact line velocity is always accompanied by the
adjustment in shape of the fluid–fluid interface when it crosses
a boundary between two different stripes. Therefore, the
stick–slip motion arises from the contrast in wetting property
(i.e. static contact angle) between the two different types of
stripes. In spite of the statistical fluctuations in MD simulations
for transient behaviors, we have excellent agreement between
the continuum and MD results, from interface shape to contact
line velocity, down to molecular length scales (a few molecular
diameters).

Induced by the switch of an *equilibrium* wetting property,
the stick–slip motion must persist for vanishingly small driving
force or average displacement velocity. Figure 9 shows
the contact line velocities for three different driving forces.
Besides the remarkable MD–continuum agreement, it is seen
that, as the driving force is gradually reduced, the velocity in
the 'plateau' region is also reduced and the dip in velocity
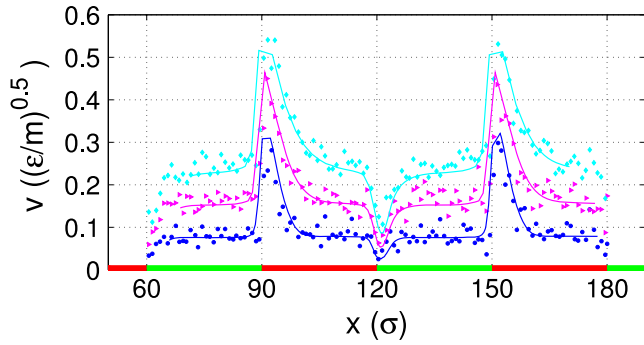
Figure 9. Contact line velocity at the lower patterned surface, plotted as a function of the contact line position, with symbols for MD results and lines for continuum results. The parameters used for interaction potentials are $\delta_{Aa} = \delta_{Bb} = \delta_{Ac} = \delta_{Bc} = 0.7$ and $\delta_{Ab} = \delta_{Ba} = 0.2$. The external force on each fluid molecule is $mg = 0.015\varepsilon/\sigma$ (diamond, cyan), $0.01\varepsilon/\sigma$ (triangle, magenta) and $0.005\varepsilon/\sigma$ (circle, blue). The distance between the bottom and top walls is $H = 17\sigma$. The pattern period is $\lambda = 60\sigma$ with $\lambda_a = \lambda_b$.

(as the interface moves from the A-like stripe to the B-like one) becomes shallower. However, the velocity peak, which appears as the interface moves from the B-like stripe to the A-like one, persists. In particular, the height of the peak, i.e. the difference between the maximum velocity and the plateau velocity, actually approaches a constant as the driving force approaches zero. Therefore, in the limit of zero driving force or average displacement velocity, the contact line velocity is everywhere close to zero except around those boundaries where the contact line is quickly driven by the switch of static contact angle

Consider an immiscible flow over a homogeneous surface with a steady displacement velocity U. The rate of energy dissipation scales as U^2 for small U according to the general rule governing the entropy production in irreversible thermodynamic processes. On patterned surfaces, however, the fluid–fluid interface has to undergo a periodic stick–slip movement with an oscillatory shape, from which extra
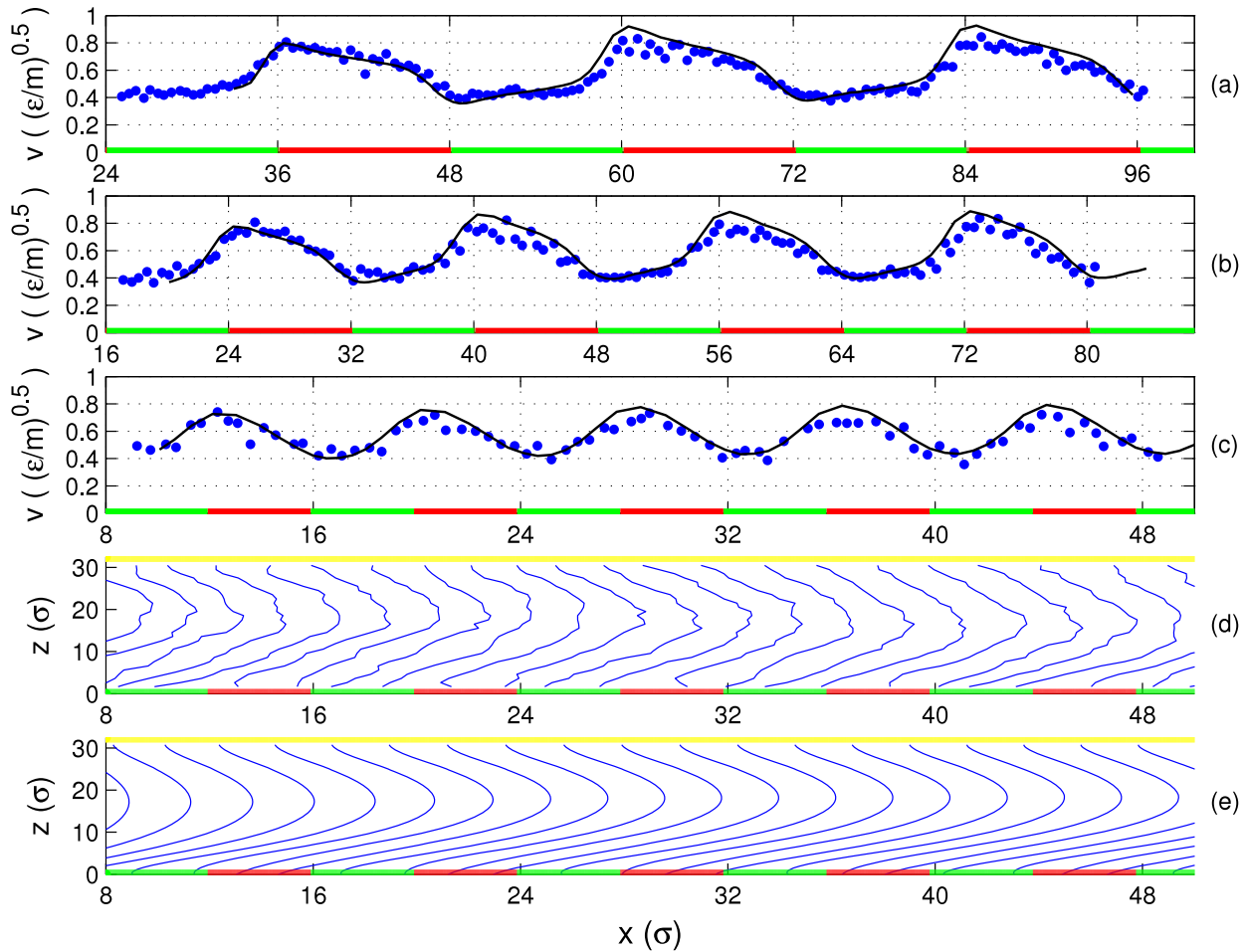
Figure 10. (a) Contact line velocity at the lower patterned surface, plotted as a function of the contact line position, with symbols for MD results and line for continuum results. The parameters used for interaction potentials are $\delta_{Aa} = \delta_{Bb} = 0.7$, $\delta_{Ab} = \delta_{Ba} = 0.3$ and $\delta_{Ac} = \delta_{Bc} = 0.5$. The external force on each fluid molecule is $mg = 0.012\varepsilon/\sigma$. The distance between the bottom and top walls is $H = 30.8\sigma$. The pattern period is $\lambda = 24\sigma$ with $\lambda_a = \lambda_b$. (b) Same as for (a) except that the pattern period is $\lambda = 16\sigma$. (c) Same as for (a) except that the pattern period is $\lambda = 8\sigma$. (d) Moving fluid–fluid interface in MD simulation. The time interval between two adjacent interfaces is 4τ. (e) Moving fluid–fluid interface in continuum calculation. The time interval between two adjacent interfaces is 3.6τ.

10

dissipation arises inevitably. For slow flows on surfaces patterned with wide stripes, the rate of energy dissipation still scales as U^2 in (wide) plateau regions of velocity (away from the boundaries between different stripes). Here U denotes the average displacement velocity. The contribution to time-integrated dissipation over a time period $T = \lambda/U$ scales as $U^2(\lambda/U) \sim U$. On the other hand, the stick–slip motion becomes independent of U as $U \to 0$ Consequently, the time-integrated extra dissipation incurred by the fluid–fluid interface crossing a boundary is independent of U. Comparing the above two contributions to time-integrated dissipation, we see that the extra dissipation dominates and the time-averaged rate of energy dissipation is linear in U to the leading order.

The adjustment of fluid–fluid interface in shape is fully manifested in slow flows on surfaces patterned with wide stripes. In particular, the timescale associated with the full interfacial adjustment is well defined in the limit of slow flows and wide stripes. When the pattern period is shortened and/or the interface displacement is quickened, the time for the interface to cover a period (i.e. λ/U) may become smaller than the time required for full interfacial adjustment. As a consequence, the interface can only partially respond to the switch of static contact angle when displaced along the patterned surface. If such partial response is further suppressed, then the interface moves as if over an almost homogeneous surface with nearly constant velocity and shape. Using both the MD and continuum results with remarkable agreement, figure 10 shows the approach to an effectively homogeneous surface as the pattern period is reduced. It is seen that the amplitude of velocity oscillation decreases with decreasing period. Moreover, the interface shape changes very little when the pattern period is small enough. Note that a relatively large distance $H = 30.8\sigma$ has been used to slow down the interfacial adjustment. Our numerical results (not presented here) also confirm that, if the pattern period is fixed, then oscillations in contact line velocity and interface shape can be suppressed as well through accelerated interface displacement.

6. Concluding remarks

Following the variational derivation of our continuum model for MCL hydrodynamics, we have presented numerical results from both continuum calculations and MD simulations for fluid velocity and fluid–fluid interface in immiscible flows past homogeneous and patterned surfaces, with remarkable quantitative agreement. This should not come as a surprise because the continuum hydrodynamics is governed by the same statistical mechanical principle as that underlying molecular dynamics, and the same (time-averaged) dynamic behavior is expected.

Compared to the steady flows past homogeneous surfaces, the transient states of immiscible flows past chemically patterned surfaces present new challenges for the test of the continuum model. First, the contact line slip velocity oscillates in both space and time. Through ensemble averaging on top of short time averaging, statistical fluctuations in MD simulations are reduced to such an extent that the oscillatory behavior

predicted by the continuum model can be clearly verified. Second, depending on the contrast in wetting property (i.e. the magnitude of contact line switch), the contact line slip velocity can be made very large momentarily by the abrupt increase of uncompensated Young stress according to the GNBC (see equations (28) and (29)). Nevertheless, our model is still able to quantitatively reproduce this fast variation over a molecular scale short distance.

Finally, we want to point out that there are limitations and inadequacies in the present approach. Our MD simulations are for the simplest monatomic fluids, and our continuum model is a minimal model, in which the density is uniform even in the interfacial region, the viscous stress is simply Newtonian and the long-range van der Waals interactions between the fluids and the solid are not included. These and other limitations and inadequacies represent work yet to be done.

References

[1] Batchelor G K 1967 *An Introduction to Fluid Dynamics* (Cambridge: Cambridge University Press)
[2] Huh C and Scriven L E 1971 *J. Colloid Interface Sci.* **35** 85
[3] Dussan V E B and Davis S H 1974 *J. Fluid Mech.* **65** 71
[4] Dussan V E B 1979 *Annu. Rev. Fluid Mech.* **11** 371
[5] de Gennes P G 1985 *Rev. Mod. Phys.* **57** 827
[6] Koplik J, Banavar J R and Willemsen J F 1988 *Phys. Rev. Lett.* **60** 1282
[7] Thompson P A and Robbins M O 1989 *Phys. Rev. Lett.* **63** 766
[8] Blake T D and Haynes J M 1969 *J. Colloid Interface Sci.* **30** 421
[9] Hocking L M 1977 *J. Fluid Mech.* **79** 209
[10] Huh C and Mason S G 1977 *J. Fluid Mech.* **81** 401
[11] Cox R G 1986 *J. Fluid Mech.* **168** 169
[12] Zhou M Y and Sheng P 1990 *Phys. Rev. Lett.* **64** 882
[13] Seppecher P 1996 *Int. J. Eng. Sci.* **34** 977
[14] Shikhmurzaev Y D 1997 *J. Fluid Mech.* **334** 211
[15] Chen H Y, Jasnow D and Vinals J 2000 *Phys. Rev. Lett.* **85** 1686
[16] Jacqmin D 2000 *J. Fluid Mech.* **402** 57
[17] Pismen L M and Pomeau Y 2000 *Phys. Rev.* E **62** 2480
[18] Briant A J and Yeomans J M 2004 *Phys. Rev.* E **69** 031603
[19] Leger L 2003 *J. Phys.: Condens. Matter* **15** S19
[20] Neto C, Evans D R, Bonaccurso E, Butt H J and Craig V S J 2005 *Rep. Prog. Phys.* **68** 2859
[21] Qian T Z, Wang X P and Sheng P 2003 *Phys. Rev.* E **68** 016306
[22] Qian T Z, Wang X P and Sheng P 2004 *Phys. Rev. Lett.* **93** 094501
[23] Qian T Z, Wang X P and Sheng P 2006 *J. Fluid Mech.* **564** 333
[24] Qian T Z, Wang X P and Sheng P 2008 *J. Fluid Mech.* **611** 333
[25] Onsager L 1931 *Phys. Rev.* **37** 405
[26] Onsager L 1931 *Phys. Rev.* **38** 2265
[27] Gau H, Herminghaus S, Lenz P and Lipowsky R 1999 *Science* **283** 46
[28] Darhuber A A, Troian S M, Miller S M and Wagner S 2000 *J. Appl. Phys.* **87** 7768
[29] Cubaud T and Fermigier M 2004 *J. Colloid Interface Sci.* **269** 171

[30] Kuksenok O, Jasnow D, Yeomans J and Balazs A 2003 *Phys. Rev. Lett.* **91** 108303

[31] Kusumaatmaja H, Leopoldes J, Dupuis A and Yeomans J 2006 *Europhys. Lett.* **73** 740

[32] Wang X P, Qian T Z and Sheng P 2008 *J. Fluid Mech.* **605** 59

[33] de Groot S R and Mazur P 1962 *Non-equilibrium Thermodynamics* (Amsterdam: North-Holland)

[34] Cahn J W and Hilliard J E 1958 *J. Chem. Phys.* **28** 258

[35] Navier C L M H 1823 *Mem. Acad. R. Sci. Inst. Fr.* **6** 389

[36] Chella R and Vinals J 1996 *Phys. Rev.* E **53** 3832

[37] Onuki A 2002 *Phase Transition Dynamics* (Cambridge: Cambridge University Press)

[38] Barrat J-L and Bocquet L 1999 *Phys. Rev. Lett.* **82** 4671

[39] Lauga E and Stone H A 2003 *J. Fluid Mech.* **489** 55

[40] Cottin-Bizonne C, Barrat J-L, Bocquet L and Charlaix E 2003 *Nat. Mater.* **2** 237

[41] Priezjev N V, Darhuber A A and Troian S M 2005 *Phys. Rev.* E **71** 041608

[42] Qian T Z, Wang X P and Sheng P 2005 *Phys. Rev.* E **72** 022501